Journal of Materials Chemistry C

ROYAL SOCIETY OF CHEMISTRY

PAPER

View Article Online
View Journal | View Issue

Cite this: J. Mater. Chem. C, 2025, 13, 4749

The effect of bipolar charge transport of derivatives of 1-phenyl-1*H*-benzo[*d*]imidazole with horizontal molecular orientation on the performance of OLEDs based on thermally activated delayed fluorescence or phosphorescence†

Simas Macionis,[a] Ehsan Ullah Rashid,[a] Jurate Simokaitiene,[a] Rita Butkute,[a] Oleksandr Bezvikonnyi,[ab] Dmytro Volyniuk,[a] Dalius Gudeika,[a] Tien-Lung Chiu,[c] Jiun-Haw Lee,[d] Zi-Wen Su,[d] Chia-Hsun Chen,[d] Ruta Budreckiene,[e] Mariia Stanitska,[a] Oleksandr Navozenko[f] and Juozas V. Grazulevicius*[a]

The synthesis and properties of two derivatives of 1-phenyl-1*H*-benzo[*d*]imidazole with differing numbers of *tert*-butylcarbazole electron-donating moieties are reported. The compounds exhibit high thermal stability, with 5% weight loss temperatures exceeding 341 °C and glass transition temperatures of over 149 °C. They display moderate triplet energies of 2.63 and 2.66 eV. The synthesized compounds were employed as host materials in phosphorescence and TADF-based organic light-emitting diodes (OLEDs). An investigation of the angle-dependent emission intensity of light-emitting layers containing the phosphorescent emitter $Ir(ppy)_2(acac)$ doped into the examined compounds revealed a notably high internal outcoupling efficiency in OLEDs, exceeding 30%. This efficiency is attributed to the significant horizontal molecular orientation factor, reaching up to 87%. Based on the characterization of the hosting properties of 1-phenyl-1*H*-benzo[*d*]imidazole derivatives, the most significant influence on device performance is attributed to their charge-transporting properties. An OLED with the phosphorescent emitter $Ir(ppy)_2(acac)$ and a host material exhibiting bipolar charge transport demonstrated an external quantum efficiency of 13%. Additionally, the picric acid sensitivity of one of the compounds was examined. Triplet-facilitated emission was completely quenched upon the addition of a nitroaromatic explosive as a guest in a film.

Received 12th November 2024,
Accepted 2nd January 2025

DOI: 10.1039/d4tc04802d

rsc.li/materials-c

1. Introduction

The technology of organic light emitting diodes (OLEDs) is undergoing rapid development owing to the advantages of color quality, response time and lower energy consumption of OLEDs when compared to competing devices in the market of display and illumination technology.[1] The singlet and triplet excitons are formed upon applying electricity in the ratio of 1 : 3 due to the spin statistics.[2,3] As a result, prompt fluorescent emitters have a limit of internal quantum efficiency (IQE) of 25%.[4] The main path to increase the efficiency of OLEDs is utilization of the triplet excited states in electroluminescence (EL), potentially increasing the IQE value to 100%. In phosphorescence OLEDs (PhOLEDs), heavy metal complexes (such as iridium or platinum complexes) which facilitate spin–orbit coupling and in turn accelerate the radiative deactivation

[a] Department of Polymer Chemistry and Technology, Faculty of Chemical Technology, Kaunas University of Technology, K. Baršausko st. 59, LT-51423, Kaunas, Lithuania. E-mail: juozas.grazulevicius@ktu.lt
[b] KTU "M-Lab" Laboratory Center, Kaunas University of Technology, Studentų g. 63A, LT-51369, Kaunas, Lithuania
[c] Department of Electrical Engineering, Yuan Ze University, Chungli, Taoyuan, 32003, Taiwan. E-mail: tlchiu@saturn.yzu.edu.tw
[d] Graduate Institute of Photonics and Optoelectronics and Department of Electrical Engineering, National Taiwan University, Taipei, 10617, Taiwan. E-mail: jiunhawlee@ntu.edu.tw
[e] Department of Biochemistry, Lithuanian University of Health Sciences, A. Mickeviciaus st. 9, LT-44307, Kaunas, Lithuania
[f] Department of Experimental Physics, Faculty of Physics, Taras Shevchenko National University of Kyiv, Akademika Glushkova Av. 4, 03127, Kyiv, Ukraine

† Electronic supplementary information (ESI) available. See DOI: https://doi.org/10.1039/d4tc04802d

through phosphorescence are utilized. Despite the increase in performance of the devices, the use of heavy metal atoms brings certain problems, such as high production costs and environmental concerns.[5–7] PhOLEDs have been developed to date, with reported external quantum efficiency (EQE) values of over 30%.[8]

OLEDs exploiting thermally activated delayed fluorescence (TADF) emerged as a promising alternative to PhOLEDs.[9] TADF is a delayed fluorescence of up-converted triplet excitons.[10] Thermal motion of atoms facilitates the reverse intersystem crossing (RISC) making delayed fluorescence possible.[11] The energy splitting between the first singlet and triplet excited states has to be low for effective RISC.[12] Thus, the design strategy for a TADF molecule is based on the separation of highest occupied and lowest unoccupied molecular orbitals (HOMO and LUMO, respectively) on separate moieties.[4] In many cases, the hybridization of locally exited (LE) and charge transfer (CT) states occurs forming new hybridized local and charge transfer (HLCT) states. The phenomenon of HLCT, as well as the hot-exciton transition, deals with the RISC at higher excited states rather than the first excited state. This leads to the emission of up-converted excitons even if the singlet–triplet energy splitting is not negligible.[3] One of the most efficient and well-studied TADF emitters 1,2,3,5-tetrakis(carbazol-9-yl)-4,6-dicyanobenzene (4CzIPN)[13] was reported to possess TADF properties operating through HLCT states.[14–16] Previously, our group reported on blue OLEDs with hosts exhibiting HLCT.[17] Specifically, OLEDs with the di-*tert*-butylcarbazole-containing TADF emitter doped into the derivative of dimethoxycarbazolyl-disubstituted dibenzofuran as a host showed an EQE value of 5.8%.[17] PhOLEDs containing imidazole derivatives with di-*tert*-butylcarbazole or carbazole moieties as HLCT-hosts exhibited EQE of up to 7.6%.[18] Bipolar or electron-transporting derivatives of carbazole and benzimidazole exhibited good performance as hosts for TADF OLEDs and PhOLEDs.[19–22] Derivatives of carbazole exhibit good hole-transporting properties and excellent thermal stability as well as exciplex-forming properties and triplet emission which can be tuned by the purposeful molecular design.[23–29] Attachment of the *tert*-butyl group to the carbazole moiety of the HLCT-TADF emitter 4CzIPN led to the improvement of the morphology of the emitting layer (EML) and enhanced OLED characteristics.[30] An electron accepting benzimidazole moiety is a promising building block for the design of donor–acceptor–donor type emitters.[31,32] Imidazole-based emitters[33–36] including derivatives of benzimidazole[37,38] are characterized by hybridization of excited states due to the twisted geometries and conformational heterogeneity. Consequently, imidazole-based compounds have been successfully applied as hosts in PhOLEDs, with relatively high EQE values of over 26%, and low efficiency roll-offs at high luminescence (Table S1, ESI†).[39]

The efficiencies of TADF-based and phosphorescence OLEDs can be improved by improving the internal outcoupling efficiency *via* molecular orientations of emitters in EMLs.[40–43] Many efficient TADF and phosphorescent emitters exhibit random molecular orientations in the EMLs.[44] Fortunately, their orientation can be improved using appropriate hosts.[45]

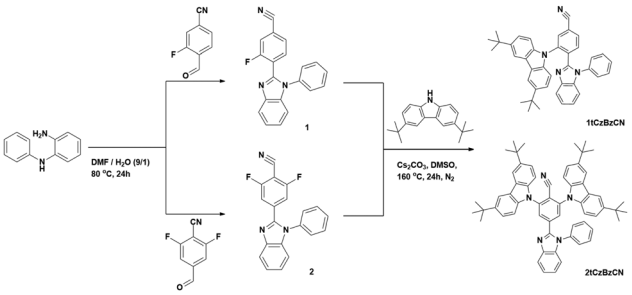

Scheme 1 Synthesis of **1tCzBzCN** and **2tCzBzCN**.

Thus, charge injecting and charge-transporting properties, triplet channel energy losses, triplet harvesting abilities, and vertical or horizontal molecular orientations should be taken into account when new hosts for TADF and phosphorescence OLEDs are being developed.[46] However, it is difficult to obtain the best combinations of properties for a single host material. In addition, it is not clear which hosting properties have the strongest influence on the performance of OLEDs. We partly aimed to study this issue by developing compounds containing the same electron-accepting unit and the different number of the same electron-donating units.

Herein, we present the synthesis and properties of the derivatives of 1-phenyl-1*H*-benzo[*d*]imidazole and di-*tert*-butylcarbazole as hosts with TADF capabilities for phosphorescence and TADF-based OLEDs. Both synthesized compounds exhibit TADF. They were tested as emitters as well as hosts in PhOLEDs and TADF-based OLEDs. As the emitter, the compound with a single di-*tert*-butylcarbazole moiety (**1tCzBzCN** in Scheme 1) showed the best performance in host-free OLEDs. Additionally, as a host, compound **1tCzBzCN** showed better performance in green phosphorescence OLEDs than compound **2tCzBzCN**. The angle-dependent photoluminescence measurements revealed the horizontal orientation factors of 0.84 for the films containing **1tCzBzCN** and 0.87 for the films containing **2tCzBzCN**. This observation suggests an enhanced outcoupling factor for the emitting layers composed of green phosphorescence emitters doped in the studied compounds. Compound **1tCzBzCN** exhibits bipolar charge carrier transport, while **2tCzBzCN** exhibits a unipolar one. Compound **1tCzBzCN** was utilized as a host for the fabrication of blue and green emitting PhOLEDs with external quantum efficiencies of 10.2 and 13%, respectively. In addition, in this study, we demonstrate the complete quenching of TADF emission of **2tCzBzCN** in a solid state by picric acid. To the best of our knowledge, this is the first report on the optical sensing of nitroaromatic explosive compounds based on TADF quenching in the solid state.

2. Experimental section

2.1 Materials

N-Phenyl-1,2-phenylenediamine, 2,6-difluoro-4-formylbenzonitrile, and 3-fluoro-4-formylbenzonitrile were purchased from Fluorochem and used as received. Dimethylformamide (DMF), dimethyl

sulfoxide (DMSO) and cesium carbonate (Cs_2CO_3) were purchased from Sigma-Aldrich and used as received. 3,6-Di-*tert*-butylcarbazole was synthesized according to the procedure reported earlier.[47] 2-Fluoro-4-benzonitril-1-phenyl-1*H*-benzo[*d*]imidazole (1, yield 70%) and 2,6-difluoro-4-benzonitril-1-phenyl-1*H*-benzo[*d*]imidazole (2, yield 47%) were synthesized from *N*-phenyl-1,2-phenylenediamine and the corresponding 4-formylbenzonitriles were synthesized according to the procedure described earlier.[48] After the initial workup, the target intermediates were recrystallized from hot methanol.

2-(3,6-Di-*tert*-butyl-9*H*-carbazol-9-yl)-4-((benzonitril)phenyl)-1-phenyl-1*H*-benzo[*d*]imidazole (1tCzBzCN). 2-Fluoro-4-benzonitril-1-phenyl-1*H*-benzo[*d*]imidazole (1) (1 g, 3.19 mmol) was added to the mixture of 3,6-di-*tert*-butylcarbazole (0.89 g, 3.19 mmol) and Cs_2CO_3 (2.1 g, 6.45 mmol) in DMSO (8 ml). The reaction mixture was stirred at 160 °C for 24 h under a nitrogen atmosphere. The reaction was monitored by TLC chromatography. Upon completion, the reaction mixture was cooled down to room temperature, the crude product was extracted with dichloromethane and dried with Na_2SO_4, and excess dichloromethane was removed *via* rotary evaporation. The crude product was purified using column chromatography on a silica gel. The mixture of tetrahydrofuran/hexane (1/4) was used as the eluent. The target compound was recrystallized from the same eluent to afford **1tCzBzCN** (0.86 g, 46%) as white crystals. T_m = 287 °C (from DSC). ^{1}H NMR (400 MHz, DMSO) δ 8.24 (d, J = 8.1 Hz, 1H), 8.16 (d, J = 8.4 Hz, 2H), 8.07 (s, 2H), 7.88 (s, 1H), 7.77 (d, J = 8.0 Hz, 1H), 7.58 (s, 1H), 7.21 (t, J = 7.7 Hz, 1H), 7.06 (m, J = 14.3, 7.5 Hz, 2H), 6.93 (t, J = 7.4 Hz, 1H), 6.85 (t, J = 8.4 Hz, 2H), 6.56 (d, J = 8.7 Hz, 2H), 6.34 (d, J = 7.6 Hz, 2H), 1.32 (s, 18H). ^{13}C NMR (101 MHz, DMSO) δ 166.39, 150.06, 142.79, 142.43, 137.99, 137.00, 136.23, 135.36, 134.22, 134.00, 130.61, 128.83, 127.87, 127.01, 126.66, 124.34, 123.37, 123.12, 122.51, 119.56, 115.82, 110.02, 108.78, 34.36, 31.73. MS (APCI+, 20 V), m/z: 572.29 $[M + NH_4]^+$.

2,6-Bis(3,6-di-*tert*-butyl-9*H*-carbazol-9-yl)-4-((benzonitrile)phenyl)-1-phenyl-1*H*-benzo[*d*]imidazole (2tCzBzCN). 2,6-Difluoro-4-benzonitril-1-phenyl-1*H*-benzo[*d*]imidazole (2) (0.47 g, 1.42 mmol) was added to the mixture of 3,6-di-*tert*-butylcarbazole (0.77 g, 2.76 mmol) and Cs_2CO_3 (1.16 g, 3.56 mmol) in DMSO (8 ml). The reaction mixture was stirred at 160 °C for 24 h under a nitrogen atmosphere. The reaction was monitored by TLC. Upon completion, the reaction mixture was cooled down to room temperature, the crude product was extracted with dichloromethane and dried with Na_2SO_4, and excess dichloromethane was removed *via* rotary evaporation. The crude product was purified using column chromatography on a silica gel. The mixture tetrahydrofuran/hexane (1/3) was used as the eluent. The target compound was recrystallized from the same eluent to afford **2tCzBzCN** (0.52 g, 37%) as yellow crystals. T_m = 412 °C (from DSC). ^{1}H NMR (400 MHz, $CDCl_3$) δ 8.11 (s, 4H), 7.94 (s, 2H), 7.83 (d, J = 7.9 Hz, 1H), 7.66–7.56 (m, 3H), 7.48 (d, J = 8.6 Hz, 4H), 7.41 (d, J = 6.9 Hz, 2H), 7.37–7.26 (m, 2H), 7.19 (d, J = 7.9 Hz, 1H), 7.10 (d, J = 8.6 Hz, 4H), 1.48 (s, 36H). ^{13}C NMR (101 MHz, $CDCl_3$) δ 148.88, 144.12, 143.33, 142.90, 138.83, 137.75, 136.91, 136.30, 130.76, 129.43, 128.21, 127.47, 124.70, 124.25, 124.10, 123.81, 120.46, 116.64, 113.45, 111.93, 110.80, 109.25, 34.83, 32.01. MS (APCI+, 20 V), m/z: 850.53 $[M + H]^+$.

3. Results and discussion

3.1 Synthetic procedures

Compounds **1tCzBzCN** and **2tCzBzCN** were synthesized in a simple two-step synthesis process (Scheme 1). In the first step, the corresponding fluoro-substituted 4-formylbenzonitriles were coupled with *N*-phenyl-1,2-phenylenediamine to form the 4-benzonitril-1-phenyl-1*H*-benzo[*d*]imidazole core and provide intermediate compounds. Following the first step, nucleophilic substitution reactions were carried out using Cs_2CO_3 as a base to introduce electron-donating 3,6-di-*tert*-butylcarbazole moieties and form the target compounds **1tCzBzCN** and **2tCzBzCN**.

3.2 Physical properties

Molecular optimization and orbitals. The electronic structures of **1tCzBzCN** and **2tCzBzCN** were optimized at their ground states at the B3LYP/6-31G** level. A notable difference in the molecular geometry of these compounds arises from the distinct dihedral angles between the benzoimidazole and benzonitrile moieties: 49° in **1tCzBzCN** and 22° in **2tCzBzCN** (Fig. 1). This variation is fundamentally attributed to the positional attachment of the benzoimidazole unit. In **1tCzBzCN**, the *ortho*-substitution places the benzoimidazole moiety in close proximity to the bulky *tert*-butylcarbazolyl group. The steric repulsion between the *tert*-butyl group and the nearby benzoimidazole moiety and benzonitrile units forces the benzoimidazole unit to adopt a significantly twisted conformation (*ca.* 49°) to alleviate the spatial strain. Conversely, in **2tCzBzCN**, the *meta*-substitution positions benzoimidazole further from the *tert*-butylcarbazole moiety, reducing steric interactions. This minimized strain enables the benzoimidazole moiety to adopt a more planar conformation relative to benzonitrile, resulting in a smaller twist (*ca.* 22°).

The molecular orbital analysis provides key insights into the electronic distribution in **1tCzBzCN** and **2tCzBzCN**. In the HOMO, the wavefunction is localized on the benzonitrile and

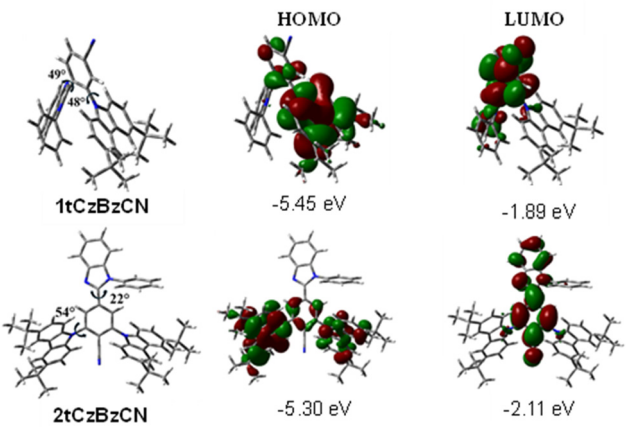

Fig. 1 Ground state optimized geometry and molecular charge distribution of **1tCzBzC** and **2tCzBzC** according to B3LYP/6-31G**.

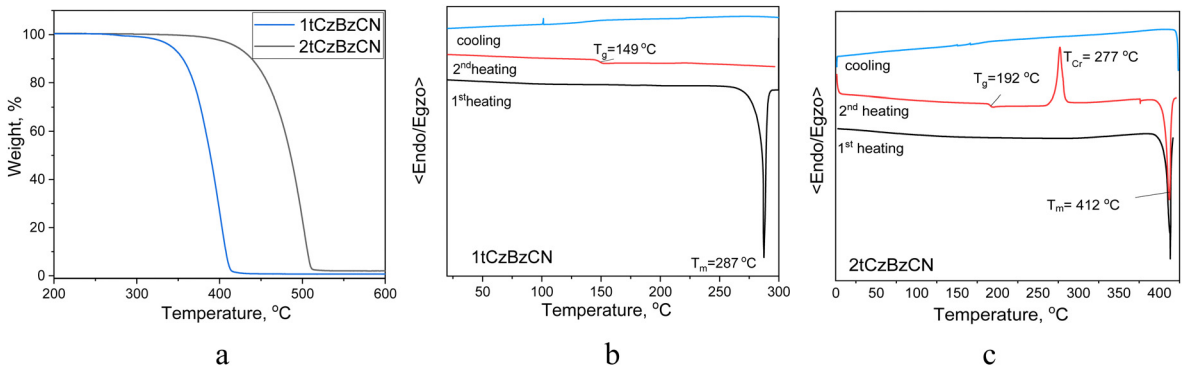

Fig. 2 TGA (a) and DSC (b) and (c) curves of **1tCzBzCN** and **2tCzBzCN**.

tert-butylcarbazole moieties in **1tCzBzCN**, while in **2tCzBzCN**, it extends over the benzonitrile and both *tert*-butylcarbazole moieties. This broader distribution in **2tCzBzCN** reflects the stronger electron-donating environment provided by the two *tert*-butylcarbazole units, which contributes to its slightly higher HOMO energy (−5.30 eV) compared to that of **1tCzBzCN** (−5.45 eV). In the LUMO, the wavefunction is predominantly localized on the benzonitrile and benzoimidazole moieties of both the compounds, highlighting the consistent electron-accepting nature of the benzonitrile unit. However, the LUMO energy of **2tCzBzCN** (−2.11 eV) is slightly lower than that that of **1tCzBzCN** (−1.89 eV). This stabilization arises from the enhanced π-conjugation between the benzonitrile and benzoimidazole units in **2tCzBzCN**, facilitated by its smaller dihedral angle (22°), which allows for an improved orbital overlap.

Thermal properties. Thermogravimetric analysis (TGA) and differential scanning colorimetry (DSC) were utilized to study the thermal properties of the synthesized compounds. TGA measurements showed that both **1tCzBzCN** and **2tCzBzCN** exhibited excellent thermal stability. Their 5% mass-loss temperatures ($T_{-5\%}$) were recorded at 341 and 426 °C, respectively (Fig. 2a and Table 1). However, the complete, single-step, loss of mass of the compounds observed during TGA measurements suggests that these values represent the temperatures corresponding to the beginning of sublimation rather than thermal degradation (Fig. 2a). Compounds **1tCzBzCN** and **2tCzBzCN** were obtained as purely crystalline compounds, and their melting temperatures (T_m) were observed at 287 and 412 °C (Fig. 2), respectively. The DSC analysis showed that both the compounds were capable of forming glasses. During the second heating scans, their glass transition temperatures (T_g) were recorded at 149 and 192 °C, respectively (Fig. 2a and c). For compound **2tCzBzCN**, the crystallization signal was recorded at 277 °C during the second heating scan, suggesting that the glassy state is not stable. The solid amorphous state of **1tCzBzCN** was more stable, as no crystallization signal was recorded in the second heating scan. The thermal characteristics of **1tCzBzCN** and **2tCzBzCN** are summarized in Table 1. Considerably higher values of T_m and T_g observed for **2tCzBzCN** relative to those of **1tCzBzCN** can be attributed to its higher molecular weight leading to stronger intermolecular interactions.

Electrochemical properties. The electrochemical properties of compounds **1tCzBzCN** and **2tCzBzCN** were studied utilizing cyclic voltammetry (CV). Ionization potential and electron affinity values were estimated from the oxidation and reduction onset potentials against ferrocene ($E_{onset}^{ox\ vs.\ Fc}$, $E_{onset}^{red\ vs.\ Fc}$), respectively. Both the synthesized compounds exhibited single oxidation peaks owing to the resident di-*tert*-butylcarbazole moieties in the molecules (Fig. 3). The ionization potential (IP_{CV}) values calculated from CV data were found to be 5.59 and 5.74 eV for compounds **1tCzBzCN** and **2tCzBzCN**, respectively. Compound **1tCzBzCN** exhibited a lower electron affinity (EA_{CV}) of 2.65 eV than **2tCzBzCN** (2.94 eV). Band gap energy values (E_{bg}) estimated using IP_{CV} and EA_{CV} were found to be 2.94 eV for **1tCzBzCN** and 2.8 eV for **2tCzBzCN**. The summary of data obtained from CV measurements is displayed in Table 1.

Photophysical properties. Absorption spectroscopy and photoluminescence (PL) spectroscopy were used to study the photophysical properties of dilute solutions and solid films of compounds **1tCzBzCN** and **2tCzBzCN**. The photophysical characteristics are displayed in Table 2. The absorption bands observed at 290 and 294 nm for the solutions of compounds **1tCzBzCN** and **2tCzBzCN**, respectively, correspond to the local

Table 1 Thermal and electrochemical characteristics of **1tCzBzCN** and **2tCzBzCN**

Compound	$T_{-5\%}$, °C	T_m, °C	T_g, °C	T_{cr}, °C	$E_{onset}^{ox\ vs.\ Fc}$, V	$E_{onset}^{red\ vs.\ Fc}$, V	IP_{CV}, eV	EA_{CV}, eV	E_{bg}, eV
1tCzBzCN	341	287	149	—	0.79	−2.15	5.59	2.65	2.94
2tCzBzCN	426	412	192	277	0.94	−1.86	5.74	2.94	2.80

$T_{-5\%}$ – 5% mass loss temperature; T_m – melting temperature; T_g – glass transition temperature; T_{cr} – crystallization temperature; E_{onset}^{ox} – onset oxidation potential *vs.* Fc measured from CV; E_{onset}^{red} – onset reduction potential *vs.* Fc measured from CV; IP_{CV} – ionization potential, calculated from $IP_{CV} = E_{onset}^{ox\ vs.\ Fc} + 4.8$; EA_{CV} – electron affinity, calculated from $EA_{CV} = E_{onset}^{red\ vs.\ Fc} + 4.8$; E_{bg} – band gap values calculated from $E_{bg} = IP_{CV} - EA_{CV}$.

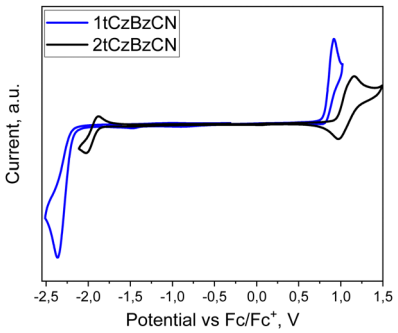

Fig. 3 CV curves of **2tCzBzCN** and **1tCzBzCN**.

transitions of benzimidazole and di-*tert*-butylcarbazole fragments.[49] The absorption bands observed in the range of 300–350 nm are related to the n–π* transitions of di-*tert*-butylcarbazole fragments, and by π–π* transition of the benzimidazole fragment.[50] The low intensity absorption band or tail (in the case of **1tCzBzCN**) observed in the range of 350–440 nm corresponds to a weak charge transfer (CT) between the di-*tert*-butylcarbazole fragment and the cyano-substituted phenyl ring.[48,51] The difference in PL spectra of the solutions of the compounds was due to the different number of electron-donating di-*tert*-butylcarbazole fragments as well as their position relative to the position of the cyano group. The absorption spectra of the films were found to be slightly bathochromically shifted in comparison to those of their solutions due to enhanced intermolecular interactions in the solid state.

PL spectra of the dilute solutions of compounds **1tCzBzCN** and **2tCzBzCN** in solvents of different polarities manifested the positive solvatochromic effect highlighting the CT nature of emission (Fig. 4a). The addition of the second di-*tert*-butylcarbazole donor moiety resulted in a redshift of PL spectra of **2tCzBzCN** when compared to **1tCzBzCN**, likely due to the extension of π-conjugation. Unlike **2tCzBzCN**, the solution of **1tCzBzCN** exhibited a redshift of 5 nm when the non-polar toluene (0.36 D) was changed to a moderately polar THF (1.75 D). An even longer bathochromic shift of 27 nm was observed when THF was changed to a highly polar DMF (3.82 D) (Fig. 4a). The increasing redshift with the increase of polarity of the solvent leads to the switch from LE character of emission to CT as for previously reported HLCT emitters.[52–55] The HLCT nature of the compounds is further substantiated by quantum chemical calculations, as elaborated later in this section. The removal of oxygen led to the enhancement of the PL only for the film of **2tCzBzCN** with a 3.3-fold increase in intensity and no additional peaks (Fig. S3, ESI†). No PL intensity increase was observed for the film of **1tCzBzCN**. The increase of PL intensity is attributed to the utilization of triplet excitons in the emission as the triplet energy is quenched in the presence of oxygen.[2] Collisional interactions with molecular oxygen could cause the drop of PLQY values for the films as the values were estimated for the samples under ambient air conditions. Deoxygenated toluene solutions of the compounds exhibited only prompt fluorescence with lifetimes of up to 10 ns (Fig. S1, ESI†). PL decay curves of the films of the compounds recorded in a vacuum were characterized by the appearance of the long-lived components of the emission with lifetimes up to 0.5 ms (Table 2 and Fig. S2, ESI†). The energy values of the first singlet S_1 and triplet T_1 excited states were estimated from the onsets of fluorescence and phosphorescence (delay of 1 ms) bands, respectively, recorded under an inert atmosphere at 77 K (Fig. 4b). These values were taken for the calculation of the singlet–triplet energy splitting (ΔE_{ST}) (Table 2). The thermal activation of delayed fluorescence was confirmed as the TADF component with sub-ms lifetimes increased upon heating (Fig. 4c). The lifetime derived from the PL decay is slightly lower for **2tCzBzCN** (0.46 ms) with ΔE_{ST} of 0.05 eV than that of **1tCzBzCN** (0.58 ms) with ΔE_{ST} of 0.33 eV. This observation shows that more efficient TADF has a shorter lifetime (Table 2).[29,56] There is experimental evidence of the HLCT nature of TADF of **1tCzBzCN**.[14,16] The relatively high ΔE_{ST} together with the undoubtfully TADF nature of emission suggests a hot exciton upconversion which occurs at higher energy levels than S_1 and T_1. The films of both compounds show no change in PL spectral behavior in the temperature range of 77 to 300 K. This indicates that the singlet excitons and the triplet excitons upconverted *via* RISC are deactivated radiatively from practically the same excited states with energy levels close to the triplet excited states from which phosphorescence occurs at low temperatures (Fig. S4, ESI†). The emission band with a vibronic substructure related to the phosphorescence disappears upon heating.

Time-dependent density functional theory (TD-DFT) calculations were performed using the LC-ω*PBE functional and the 6-31G** basis set to get insightful aspects of excited state properties. The range separation parameter "ω" is tuned for the gaseous medium. The tuned ω value is 0.178 $Bohr^{-1}$ for **1tCzBzCN** and 0.155 $Bohr^{-1}$ for **2tCzBzCN**. The theoretical vertical excited-state energies were adjusted by applying a redshift of 0.4 eV for **1tCzBzCN** and 0.2 eV for **2tCzBzCN** (as summarized in Table S2, ESI†) to achieve closer alignment with experimental results. This adjustment effectively accounts for the influence of the molecular environment, providing a more accurate depiction of the excited-state dynamics. The TD-DFT calculations unveiled the presence of four triplet states (T_1–T_4) lying below the S_1 in **1tCzBzCN**, highlighting the potential for

Table 2 Major photophysical characteristics of the dilute toluene solutions and the films of compounds **1tCzBzCN** and **2tCzBzCN**

Compounds	$PLQY_{tol}$[a]	$PLQY_{film}$[b]	$PLQY_{doped}$[c]	S_1, eV[d]	T_1, eV[d]	ΔE_{ST}, eV[d]	τ_1, ns[ae]	τ_2, ms[bf]
1tCzBzCN	0.26	0.20	0.63	2.99	2.66	0.33	4.22, 10.11	0.58
2tCzBzCN	0.09	0.39	0.48	2.68	2.63	0.05	1.85, 4.03	0.46

[a] Toluene solutions at room temperature in air. [b] Neat films at room temperature in air. [c] Films of the molecular mixtures with $Ir(ppy)_2(acac)$ (10 wt%) at room temperature in air. [d] Films at 77 K temperature under an argon atmosphere. [e] Lifetime of prompt fluorescence at room temperature, in air. [f] Lifetime of delayed fluorescence at room temperature, in a vacuum.

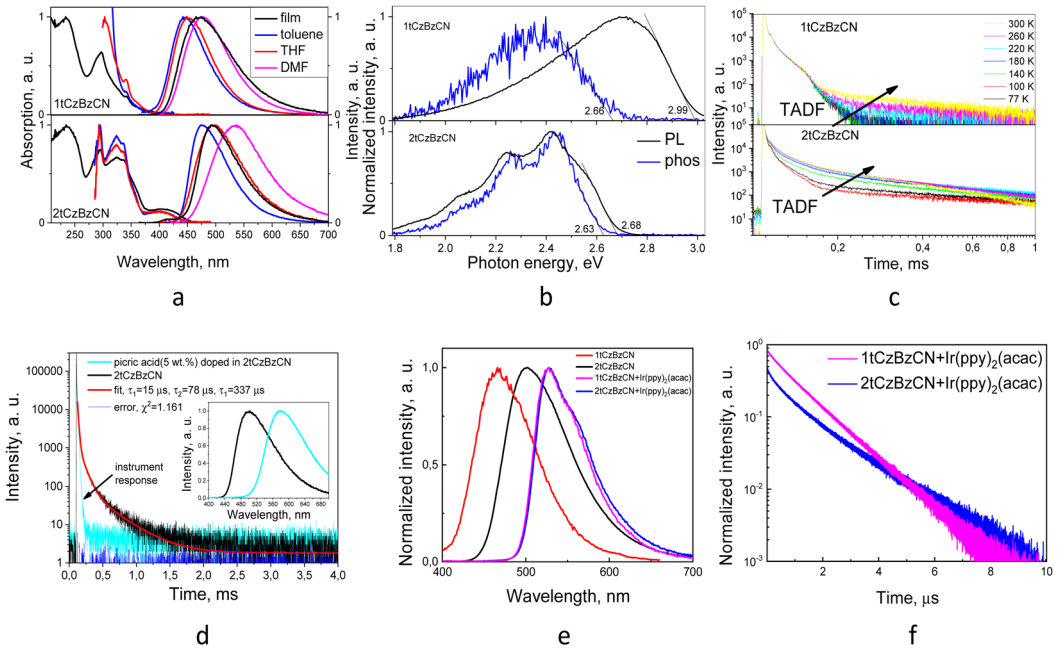

Fig. 4 Absorption and PL spectra of the films and dilute toluene, THF and DMF solutions (a); PL and phosphorescence spectra, recorded at 77 K of the films (b); PL decay curves, recorded at different temperatures of the films (c) of compounds **1tCzBzCN** and **2tCzBzCN**. PL decay curves of the films of the mixtures of picric acid (5 wt%) doped in **2tCzBzCN** recorded at room temperature in a vacuum. Inset: PL spectra of the films (d). PL spectra (e), PL decay curves (f), recorded at room temperature of the films of the molecular mixtures of $Ir(ppy)_2acac$ (10 wt%) and compounds **1tCzBzCN** and **2tCzBzCN**.

hot exciton RISC due to multiple intermediate triplet levels. To unravel the nature of these excitations, the natural transition orbitals (NTOs) were generated (Fig. S5, ESI†). The NTOs of S_1 exhibit a combination of localization on the benzonitrile moiety and CT from the *tert*-butylcarbazole moiety to the benzoimidazole fragment. This observation is consistent with the HLCT nature of the S_1 state. The T_1 and T_3 states share the similar excitation pattern, showing localization on benzonitrile and benzoimidazole units with CT from the *tert*-butylcarbazole moiety. In contrast, T_2 is predominantly localized on the *tert*-butylcarbazole unit, while T_4 shows a mixed localization on the benzonitrile and *tert*-butylcarbazole moieties. Despite the highest spin–orbit coupling (SOC) value between S_1 and T_1 (0.70 cm^{-1}, Fig. S6, ESI†), the significant $\Delta E_{(S_1-T_1)}$ gap (0.4 eV) renders the S_1–T_1 pathway thermodynamically unfavourable for efficient RISC. However, T_4 emerges as a viable mediator in the hot exciton RISC. T_4 exhibits the smallest energy gap with S_1 (0.03 eV) and the second-highest SOC value (0.24 cm^{-1}) for the S_1–T_4 pathway. Additionally, the T_4–T_3 energy gap (0.1 eV) is larger than the S_1–T_4 gap, reducing the likelihood of internal conversion and favouring RISC as the dominant process.

The NTOs for the S_1 state of **2tCzBzCN** reveal a characteristic HLCT nature, with electronic density localized on the benzonitrile moiety and charge transfer from the *tert*-butylcarbazole to the acceptor units. Similarly, the T_1 state shows predominant localization on the benzonitrile moiety, minor contributions from the benzoimidazole unit, and charge transfer from the *tert*-butylcarbazole fragment to the acceptor moieties. In the T_2 state, the NTOs depict a mixture of localization on benzonitrile and benzoimidazole units with charge transfer from one of the *tert*-butylcarbazole moieties. This variation in orbital character for both T_1 and T_2, compared to S_1, enables both states to act as potential pathways for RISC. Among these, the S_1–T_2 pathway is characterized by a small energy gap but exhibits a low SOC value, indicating that this pathway is relatively weak for RISC. In contrast, the S_1–T_1 pathway, with a moderate theoretical energy gap of 0.15 eV, demonstrates the significantly higher SOC value (0.90 cm^{-1}), marking it as the dominant and highly efficient pathway for RISC. The pronounced SOC value for the S_1–T_1 pathway translates to a faster RISC rate in **2tCzBzCN**, facilitating efficient conversion of triplet excitons to singlet states. These dynamics contribute to the shorter PL lifetime of **2tCzBzCN**, compared to that of its counterpart (**1tCzBzCN**).

Additionally, the sensitivity of TADF of compound **2tCzBzCN** to the presence of nitroaromatic explosive compounds was examined. Expectedly, the film of picric acid was found to be non-emissive. The PL spectra and PL decay curves of the film of the molecular mixture of picric acid (5 wt%) and **2tCzBzCN** are shown in Fig. 4d. For comparison, the PL spectrum of the film of neat **2tCzBzCN** is shown. The peak of the PL spectrum of the molecular mixture of **2tCzBzCN** and picric acid appeared at 578 nm. It was considerably redshifted with respect to the peak of the PL spectrum of the neat layer of **2tCzBzCN** which was observed at 500 nm. The bathochromic shift is explained by intermolecular interactions of the two compounds. Electronic excitation energy transfer occurs between the host and the guest effectively quenching TADF. Consequently, the long-lived component of TADF with a lifetime of up to 0.34 ms was eliminated in the PL decay curve of the molecular mixture of **2tCzBzCN** and picric acid. Only prompt fluorescence was

observed when picric acid was added (5 wt%). At a higher concentration of picric acid of 25 wt%, the host–guest system became non-emissive demonstrating that picric acid totally quenched prompt fluorescence as well as TADF. To gain insights into the interaction mechanism between **2tCzBzCN** and picric acid, quantum chemical calculations were conducted at the LC-ωPBE/6-31G** theoretical level. The optimized geometry of the complex of **2tCzBzCN** and picric acid is shown in Fig. S7 (ESI†). It highlights the spatial arrangement of the interacting species. The molecular orbitals of the complex show that the HOMO is primarily localized on the electron-rich *tert*-butylcarbazole moieties of **2tCzBzCN**, while the LUMO is concentrated on the highly electron-deficient trinitrophenol (picric acid). This clear transfer of charge density from **2tCzBzCN** to picric acid signifies strong non-covalent interactions. This charge transfer mechanism plays a pivotal role in modulating the exciton dynamics, providing a theoretical basis for the observed quenching of emission of **2tCzBzCN** by picric acid. The quantum chemical calculations further confirm a substantial interaction energy of -8.03 kcal mol^{-1}, indicating that the formation of the complex is both thermodynamically favourable and spontaneous.

The solid films of emitters **1tCzBzCN** and **2tCzBzCN** at room temperature in air demonstrated relatively low photoluminescence quantum yields of 0.2 and 0.39. To pursue efficient OLED performance, it is necessary to add efficient emitters to enhance the formation of excitons. Before device fabrication, the energy transfer between the host and the dopant was analyzed using PL spectra and PL decay curves of vacuum-deposited layers of **1tCzBzCN** and **2tCzBzCN**, and their molecular mixtures with 10 wt% bis[2-(2-pyridinyl-*N*)phenyl-C]-(acetylacetonato)iridium(III) ($Ir(ppy)_2acac$) ($S_1 \sim 2.47$ eV and $T_1 \sim 2.45$ eV). The PL spectra and PL decay curves are shown in Fig. 4e and f and Fig. S2 (ESI†). The whole PL spectra of the molecular mixtures are attributed to the emission of $Ir(ppy)_2acac$, illustrating the efficient energy transfer from the hosts (**1tCzBzCN** or **2tCzBzCN**) to the guest ($Ir(ppy)_2acac$). The yields are 0.63 for the mixture containing **1tCzBzCN** and 0.48 for the mixture containing **2tCzBzCN** (Fig. S8, ESI†). TPL decay curves of the layers of **1tCzBzCN** and **2tCzBzCN** shown in Fig. S2 (ESI†) exhibit long lived components with the lifetimes of over 4 ms, which evidence the possibility of ISC or RISC. After mixing the synthesized compounds with $Ir(ppy)_2acac$, long lived components disappeared in the PL decay curves (Fig. 4f). They revealed emission lifetimes of less than 10 μs. This observation leads to a conclusion that $Ir(ppy)_2acac$ facilitates exciton emission, corresponding to the increased PLQY. The PL decay curve of the molecular mixture of **1tCzBzCN** and $Ir(ppy)_2acac$ is characterized by the single exponential function, indicating efficient energy transfer from the host to the dopant, leading to the enhancement of PLQY up to 0.63. This may result from very fast and efficient Förster energy transfer (FRET) and Dexter energy transfer (DET) between the host and the guest. On the other hand, for the adequate representation of the PL decay curve of the molecular mixture of **2tCzBzCN** and $Ir(ppy)_2acac$, the double exponential fit was required. This observation can be attributed to the ISC process, implying a relatively slow or inefficient FRET between the host and the dopant. This resulted in a lower PLQY of 0.48.

Charge-transporting properties. The charge-transporting properties of vacuum-deposited films of **1tCzBzCN** and **2tCzBzCN** were investigated by conducting time-of-flight (TOF) measurements (Fig. 5 and Fig. S9, ESI†). The typical two-electrode structure ITO/film/Al of TOF samples with one optically transparent electrode indium–tin oxide (ITO) was used. The thicknesses (d) of the films were measured using a profilometer Profilm3D (Fig. S10, ESI†). The TOF samples were excited by a 350 nm laser beam through the ITO side. The positive or negative voltages were selectively applied to ITO, simultaneously recording the TOF photocurrent transients for holes or electrons, respectively (Fig. 5a–c and Fig. S9, ESI†). From the TOF current transients plotted in log–log scales, the transit times (t_{tr}) for holes and electrons were estimated for **1tCzBzCN** (Fig. 5a and b). For the films of **2tCzBzCN** t_{tr} values only for holes were obtained (Fig. 5c and Fig. S9, ESI†). Thus, **1tCzBzCN** exhibited bipolar charge carrier transport, whereas **2tCzBzCN** showed only hole-transporting properties. Charge carrier mobility dependences on the electric field were adequately expressed using a Poole–Frenkel function $\mu_{e,h} = \mu_{0e,h}^{(\beta e,h \cdot E1/2)}$. Here, $\mu_{e,h}$ are hole and electron mobilities at different electric fields (E), $\mu_{0e,h}$ are hole and electron mobilities at E of equal to zero, $\beta_{e,h}$ is the Poole–Frenkel factor for holes or electrons (Fig. 5d). The samples of compounds **1tCzBzCN** and **2tCzBzCN** showed very close μ_{0h} values of 7.5×10^{-10} and 9.1×10^{-10} cm^2 V^{-1} s^{-1}, respectively. The slightly different β_h values of 0.0086 and 0.0074 cm$^{1/2}$ V$^{-1/2}$

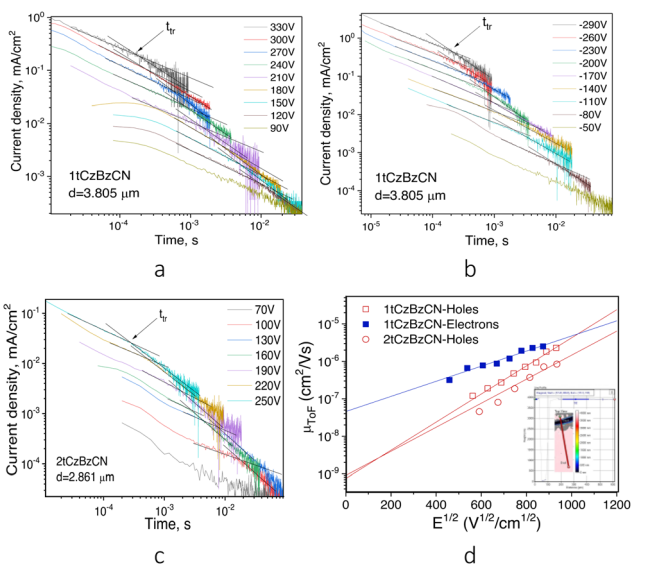

Fig. 5 TOF transients of vacuum-deposited films of compounds **1tCzBzCN** (a) and (b) and **2tCzBzCN** (c) under applied positive voltages for holes and negative voltages for electrons at an optically transparent electrode ITO and the corresponding charge carrier mobilities (d) as the Poole–Frenkel function of electric fields. Inset: A fragment of data of thickness measurements of compound **1tCzBzCN** using a profilometer Profilm3D.

were observed for **1tCzBzCN** and **2tCzBzCN**, respectively, resulting in the considerable difference of μ_h values (2.34×10^{-6} and 8.75×10^{-7} $cm^2 V^{-1} s^{-1}$ at E of 8.7×10^5 $V cm^{-1}$). Such a difference could be attributed to the twice the number of *tert*-butyl groups in **2tCzBzCN**. Apparently, *tert*-butyl groups may hinder HOMO–HOMO overlapping of neighbouring molecules of **2tCzBzCN** in vacuum-deposited films thus reducing its hole mobility in comparison to that of **1tCzBzCN**. In addition, the higher number of *tert*-butyl groups in **2tCzBzCN** may prevent LUMO–LUMO overlapping of its neighbouring molecules. Our presumption is supported by previous reports on the different HOMO–LUMO separations of donor–acceptor type compounds caused by only slight modification of the substituents on the donor moieties.[24,57] In addition, molecular packing of the molecules of **1tCzBzCN** and **2tCzBzCN** in their films should be different, leading to the different HOMO–HOMO and LUMO–LUMO overlapping of neighbouring molecules. This results in the different charge-transporting properties of the films of **1tCzBzCN** and **2tCzBzCN**. As a result, **2tCzBzCN** did not exhibit electron transport. The sample **1tCzBzCN** showed electron transporting properties with μ_{0e} of 4.6×10^{-8} $cm^2 V^{-1} s^{-1}$, β_e of 0.0047 $cm^{1/2} V^{-1/2}$ and μ_e of 3.58×10^{-6} $cm^2 V^{-1} s^{-1}$ at E of 8.7×10^5 $V cm^{-1}$ (Fig. 5d).

3.3 Performance of organic light-emitting diodes

The series of OLEDs with the structure ITO/TAPC (50 nm)/mCP (10 nm)/EML (30 nm)/DPPS (55 nm)/LiF/Al were fabricated. ITO and Al were anode and cathode electrodes, respectively. The layers of 1,1-bis[(di-4-tolylamino)phenyl]cyclohexane (TAPC) and diphenyl-bis[4-(pyridin-3-yl)phenyl]silan (DPPS) were selected as hole and electron transport layers, respectively. *N*,*N*-Dicarbazolyl-3,5-benzene (mCP) was utilized for the deposition of the exciton blocking layer. LiF was utilized as the electron injection layer. As the light-emitting layer (EML), the neat layers of **1tCzBzCN** (devices A), **2tCzBzCN** (devices C) or the layers of **1tCzBzCN** (devices B, E and F) and **2tCzBzCN** (device D) co-deposited with the different guests were used. Green phosphorescent emitter $Ir(ppy)_2(acac)$ (10 wt%) was used as a guest for the fabrication of OLEDs B and D. Sky-blue phosphorescent emitter bis[2-(4,6-difluorophenyl)pyridinato-C_2,*N*] (picolinato)iridium(III) (FIrpic) (9 wt%) was used as a guest in device E. The green TADF emitter 1,2,3,5-tetrakis(carbazol-9-yl)-4,6-dicyanobenzene (4CzIPN) was used as a guest in device F. The heterostructure of OLEDs and the molecular structures of the functional compounds are presented in Fig. 6a and b.

The EL spectra of devices A and C employing EMLs of neat compounds **1tCzBzCN** and **2tCzBzCN** correspond well with the PL spectra of the films of the respective compounds. The higher PLQY was observed for the film of **2tCzBzCN** than for the film of **1tCzBzCN** (Table 3). OLED A with the EML of **1tCzBzCN** demonstrated more than twice as high external quantum efficiency compared to that of the **2tCzBzCN**-based device (C). Thus, usage of **1tCzBzCN** containing one electron-donating substituent allowed reaching the considerably higher external quantum efficiency of OLEDs compared to that of the device with **2tCzBzCN** containing two di-*tert*-butylcarbazole moieties. This is due to the charge imbalance caused by **2tCzBzCN** which also explains significantly higher turn-on and lit-on voltages of OLED C when compared to those of OLED A (Fig. 5d and 6d). Together with the PL data of guest–host systems, this observation points to **1tCzBzCN** being a more efficient host than **2tCzBzCN**. Among OLEDs based on $Ir(ppy)_2(acac)$, the device with **1tCzBzCN** has superior values of current efficiency (CE), power efficiency (PE) and EQE relative to OLEDs with **2tCzBzCN**. For the estimation of the performance of **1tCzBzCN**

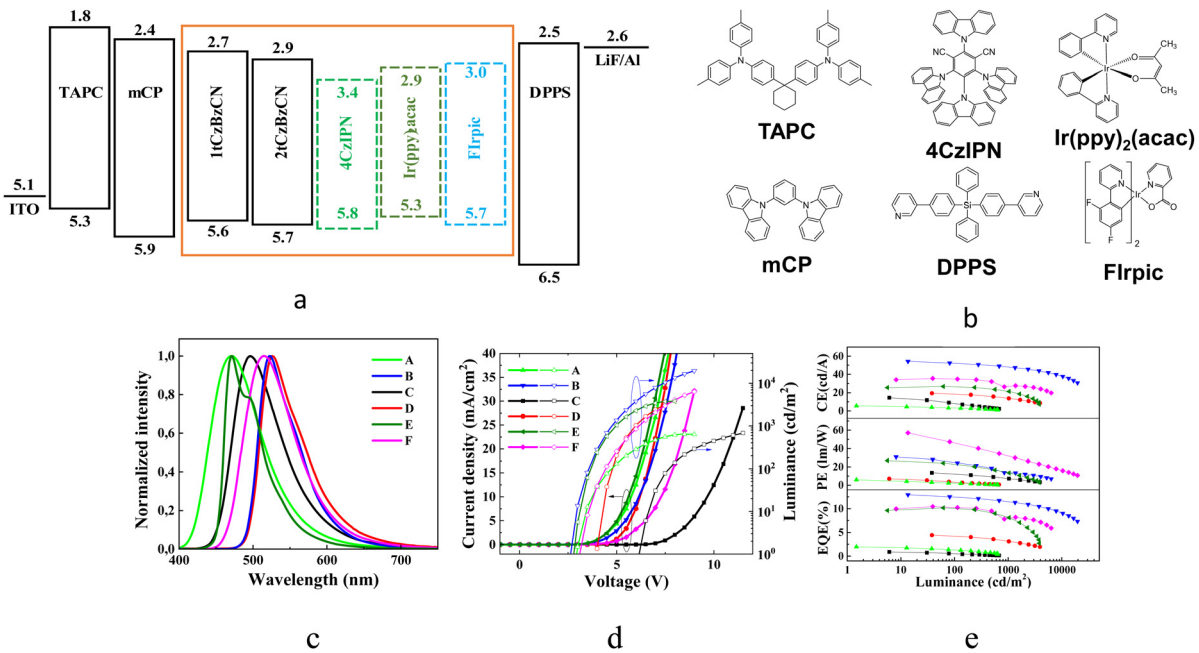

Fig. 6 The general structure of the fabricated OLEDs (a). The chemical structures of the functional compounds (b). EL spectra (c), current density–luminance–voltage (d) and CE–PE–EQE–luminance plots (e).

Table 3 EL characteristics of OLEDs

Device	EML	V_{on}[a], V	CE[b], cd A^{-1}	PE[b], lm W^{-1}	EQE[b], %	λ, nm	1931 CIEx,y
A	**1tCzBzCN**	4.0/3.0	5.6/2.1/—	5.9/3.2/—	2.0/1.3/—	472	(0.19, 0.31)
B	**1tCzBzCN** – Ir(ppy)$_2$(acac)	4.3/2.6	54.3/53.8/48.1	57/46.3/32.1	13.0/12.4/11.47	522	(0.31, 0.64)
C	**2tCzBzCN**	7.6/6.2	14.5/8.23/—	7.0/3.3/—	0.9/0.5/—	496	(0.22, 0.48)
D	**2tCzBzCN** – Ir(ppy)$_2$(acac)	4.9/4.0	19.4/18.8/13.8	13.6/12.7/7.3	4.4/4.3/3.2	526	(0.35, 0.62)
E	**1tCzBzCN** – FIrpic	4.0/2.8	25.6/25.8/21.4	26.8/22.5/13.4	10.2/10.0/7.9	472	(0.15, 0.32)
F	**1tCzBzCN** – 4CzIPN	5.2/3.1	35.6/34.1/26.7	30.7/24.7/13.7	10.4/10.2/7.88	514	(0.28, 0.58)

[a] Turn-on voltage at 1 mA cm^{-2} and the lit-on voltage 1 cd m^{-2}. [b] Maximum value/at 100 cd m^{-2}/at 1000 cd m^{-2}.

as a host, OLEDs E and F utilizing FIrpic and 4CzIPN as emitters, were fabricated and characterized. OLEDs with EMLs based on guest–host systems showed EL spectra representing the emission of the guests without the EL contribution of the host.

Time-resolved electroluminescence (TREL) spectra of devices A and C based on EMLs of the neat compounds have characteristic spikes due to imperfect charge transport at recombination sites. The inset of Fig. 7 a is an enlarged view of the spikes, which reflect a great deal of trap states inside the layer of **2tCzBzCN** which impede charge carrier transport, prevent charge carrier recombination, and degrade the device performance. While device B has a long lifetime of emission, the TREL signal is shortened in comparison to that of OLED D, highlighting more efficient energy transfer. FIrpic and **1tCzBzCN** have similar wavelengths of the EL peaks which are conventionally viewed as unfavorable for efficient host–guest interactions. Nevertheless, the long radiative lifetime of emission of OLED E (Fig. 7b) makes it possible to facilitate FRET even with a small spectral overlap of emission spectrum of the host and the absorption band of the guest due to vibronic coupling.[58] Thus, OLED F based on green emitting 4CzIPN, and E based on sky-blue emitting FIrpic showed close values of maximum EQE of *ca.* 10%. For further investigation of the output coupling effect of devices B and D, the angle-dependent PL measurements were performed. They allow studying the optical transition dipole of the systems of Ir(ppy)$_2$(acac) doped in **1tCzBzCN** and **2tCzBzCN** *via* a laser (excitation at 325 nm) and collecting *p*-polarized fluorescence intensities at different emission angles as shown in Fig. 7. Two ideal cases, such as the molecular arrangement in a perfect horizontal orientation factor (Θ of 1) and an isotropic dipole orientation factor (Θ of 0.66), were also simulated to be the baseline in comparison to the experimental angle-dependent PL profiles. After fitting the two main peaks of the experimental angle-dependent PL spectra, high Θ values of 0.84 and 0.87 were obtained for OLEDs B and D, respectively. This indicates that the EMLs of devices B and D provide potentially high outcoupling efficiency of more than 30%. Device B showed a maximum EQE of 13%. This value correlates with the PLQY of the film of the corresponding guest–host system.

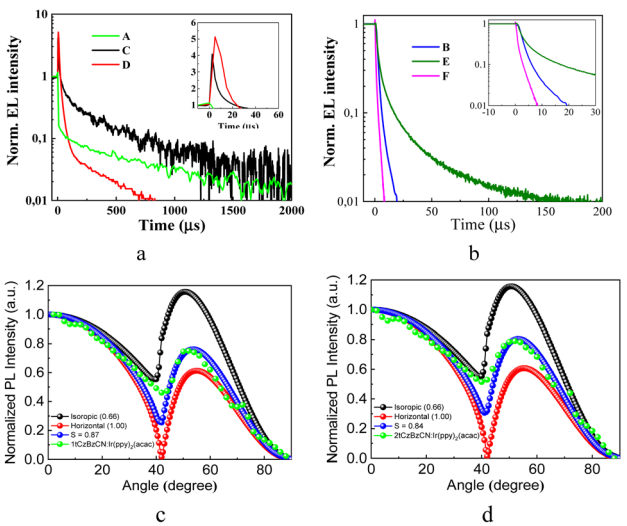

Fig. 7 TREL signals of OLEDs A, C, and D (a) and B, E, and F (b) Inset: an enlarged view of the spikes. Simulated (Θ of 1, 0.66), experimental, and fitting (Θ = 0.92) angle-dependent PL intensity profiles of the films of the molecular mixtures of Ir(ppy)$_2$acac (10 wt%) and compounds **1tCzBzCN** (c) and **2tCzBzCN** (d).

4. Conclusions

Two derivatives with 1-phenyl-1*H*-benzo[*d*]imidazole and di-*tert*-butylcarbazole groups were synthesized and analyzed for their potential as hosts for OLEDs with TADF capabilities. TADF of **2tCzBzCN** was completely quenched by the addition of picric acid due to electronic excitation energy transfer. This demonstrates the great potential of TADF for optical sensing of nitroaromatic explosives. TADF of the synthesized emitters originates from the hybridization of local excited and charge transfer states. The solid films of the compounds show moderate values of photoluminescence quantum yields of up to 39%. The derivative of 1-phenyl-1*H*-benzo[*d*]imidazole with the single *tert*-butylcarbazolyl group performs better in organic light emitting diodes than the derivative with two *tert*-butylcarbazolyl groups. The effective electronic excitation energy transfer from the host to the guest is achieved due to vibronic coupling. The angle-dependent photoluminescence measurements performed for the films of the molecular mixtures of the compounds with the green phosphorescent emitter revealed the horizontal orientation factors of 0.84 and 0.87, suggesting enhanced out-coupling factors for the emitting layers. The performance of the compounds in OLEDs is primarily influenced by their charge-transport characteristics. The derivative of phenyl-1*H*-benzo[*d*]imidazole with the single *tert*-butylcarbazolyl group with hole and electron mobilities of 2.34 $\times$ 10^{-6} and 3.58 $\times$ 10^{-6} cm^2 V^{-1} s^{-1}, respectively, at an electric

field of 8.7 × 10^5 V cm^{-1} exhibited the best performance. OLEDs with this compound as a host showed an external quantum efficiency of 13%. The results of this study show that the search for hosts with high and balanced hole and electron mobilities, together with high internal outcoupling efficiency and triplet harvesting ability can result in the development of OLEDs with high external quantum efficiency.

Author contributions

Conceptualization: Simas Macionis, Jurate Simokaitiene, and Dalius Gudeika; methodology and investigation: Simas Macionis, Oleksandr Bezvikonnyi, Ehsan Ullah Rashid, Jiun-Haw Lee, Zi-Wen Su, Chia-Hsun Chen, Mariia Stanitska, and Oleksandr Navozenko; validation and data curation: Rita Butkute, Ruta Budreckiene, and Dmytro Volyniuk; formal analysis and writing of original draft: Simas Macionis, Jurate Simokaitiene, Oleksandr Bezvikonnyi, Dmytro Volyniuk, and Ehsan Ullah Rashid; writing – review and editing: Tien-Lung Chiu and Juozas. V. Grazulevicius; supervision and funding acquisition: Oleksandr Navozenko and Juozas. V. Grazulevicius.

Data availability

The data supporting this article have been included as part of the ESI.†

Conflicts of interest

There are no conflicts to declare.

Acknowledgements

This project has received funding from the Research Council of Lithuania (LMTLT), project ''Exploitation of the solid-state enhanced long-lived emission of organic emitters for the detection of nitroaromatic explosive compounds'', agreement no. S-LU-24-6. J. H. Lee acknowledges the support and funding from the NSTC, grants 113-2221-E-002-102-MY3 and 112-2221-E-002-216-MY3. T. L. Chiu acknowledges the support and funding from the NSTC, grants 113-2622-E-155-002 and 112-2221-E-155-028-MY3.

References

1 E. Tankelevičiūtė, I. D. W. Samuel and E. Zysman-Colman, *J. Phys. Chem. Lett.*, 2024, **15**, 1034–1047.
2 T. Serevičius, R. Skaisgiris, G. Kreiza, J. Dodonova, K. Kazlauskas, E. Orentas, S. Tumkevičius and S. Juršenas, *J. Phys. Chem. A*, 2021, **125**, 1637–1641.
3 S. W. Park, D. Kim and Y. M. Rhee, *Int. J. Mol. Sci.*, 2023, **24**, 12362.
4 Y. Im, M. Kim, Y. J. Cho, J. A. Seo, K. S. Yook and J. Y. Lee, *Chem. Mater.*, 2017, **29**, 1946–1963.
5 H. Yersin and W. J. Finkenzeller, *Triplet Emitters for Organic Light-Emitting Diodes: Basic Properties*, John Wiley & Sons, Ltd, 2008.
6 H. Yersin, *Triplet Emitters for OLED Applications. Mechanisms of Exciton Trapping and Control of Emission Properties*, Springer, Berlin, Heidelberg, 2012.
7 A. Jana, V. G. Sree, Q. Ba, S. C. Cho, S. U. Lee, S. Cho, Y. Jo, A. Meena, H. Kim and H. Im, *J. Mater. Chem. C*, 2021, **9**, 11314–11323.
8 J. Jayabharathi, V. Thanikachalam and S. Thilagavathy, *Coord. Chem. Rev.*, 2023, **483**, 215100.
9 J. Cameron, A. Klimash, E. J. Hussien, F. Hacivelioğlu and P. J. Skabara, *Sustainable Strategies in Organic Electronics*, 2022, pp. 229–280.
10 A. Endo, K. Sato, K. Yoshimura, T. Kai, A. Kawada, H. Miyazaki and C. Adachi, *Appl. Phys. Lett.*, 2011, **98**, 083302.
11 B. Zhou, D. Yan, B. Zhou and D. Yan, *Adv. Funct. Mater.*, 2019, **29**, 1807599.
12 M. Chapran, P. Pander, M. Vasylieva, G. Wiosna-Salyga, J. Ulanski, F. B. Dias and P. Data, *ACS Appl. Mater. Interfaces*, 2019, **11**, 13460–13471.
13 H. Uoyama, K. Goushi, K. Shizu, H. Nomura and C. Adachi, *Nature*, 2012, **492**, 234–238.
14 H. Nakanotani, Y. Tsuchiya and C. Adachi, *Chem. Lett.*, 2021, **50**, 938–948.
15 T. Hosokai, H. Matsuzaki, H. Nakanotani, K. Tokumaru, T. Tsutsui, A. Furube, K. Nasu, H. Nomura, M. Yahiro and C. Adachi, *Sci. Adv.*, 2017, **3**, e1603282.
16 H. Noda, X. K. Chen, H. Nakanotani, T. Hosokai, M. Miyajima, N. Notsuka, Y. Kashima, J. L. Brédas and C. Adachi, *Nat. Mater.*, 2019, **18**, 1084–1090.
17 O. Bezvikonnyi, D. Gudeika, D. Volyniuk, A. Bucinskas and J. V. Grazulevicius, *Mater. Sci. Eng., B*, 2021, **273**, 115441.
18 O. Bezvikonnyi, R. S. Bernard, V. Andruleviciene, D. Volyniuk, R. Keruckiene, K. Vaiciulaityte, L. Labanauskas and J. V. Grazulevicius, *Materials*, 2022, **15**, 8495.
19 Z. J. Gao, T. H. Yeh, J. J. Xu, C. C. Lee, A. Chowdhury, B. C. Wang, S. W. Liu and C. H. Chen, *ACS Omega*, 2020, **5**, 10553–10561.
20 J. J. Huang, Y. H. Hung, P. L. Ting, Y. N. Tsai, H. J. Gao, T. L. Chiu, J. H. Lee, C. L. Chen, P. T. Chou and M. K. Leung, *Org. Lett.*, 2016, **18**, 672–675.
21 S. Y. Chang, G. T. Lin, Y. C. Cheng, J. J. Huang, C. L. Chang, C. F. Lin, J. H. Lee, T. L. Chiu and M. K. Leung, *ACS Appl. Mater. Interfaces*, 2018, **10**, 42723–42732.
22 Y. M. Chen, W. Y. Hung, H. W. You, A. Chaskar, H. C. Ting, H. F. Chen, K. T. Wong and Y. H. Liu, *J. Mater. Chem.*, 2011, **21**, 14971–14978.
23 C. Li, C. Duan, C. Han, H. Xu, C. Li, C. Duan, C. Han and H. Xu, *Adv. Mater.*, 2018, **30**, 1804228.
24 C.-Y. Chan, L.-S. Cui, J. Uk Kim, H. Nakanotani, C. Adachi, C. Chan, L. Cui, J. U. Kim, H. Nakanotani and C. Adachi, *Adv. Funct. Mater.*, 2018, **28**, 1706023.
25 S. M. Bonesi, M. Mesaros, F. M. Cabrerizo, M. A. Ponce, G. M. Bilmes and R. Erra-Balsells, *Chem. Phys. Lett.*, 2007, **446**, 49–55.

26 H. Ikebe, K. Nakao, E. Hisamura, M. Furukori, Y. Nakayama, T. Hosokai, M. Yang, G. Liu, T. Yasuda and K. Albrecht, *Aggregate*, 2024, **5**, e405.
27 P. Ledwon, P. Zassowski, T. Jarosz, M. Lapkowski, P. Wagner, V. Cherpak and P. Stakhira, *J. Mater. Chem. C*, 2016, **4**, 2219–2227.
28 A. Kadashchuk, Y. Skryshevski, A. Vakhnin, S. Toliautas, J. Sulskus, R. Augulis, V. Gulbinas, S. Nespurek, J. Genoe and L. Valkunas, *J. Phys. Chem. C*, 2014, **118**, 22923–22934.
29 Y. A. Skryshevski and A. Y. Vakhnin, *Ukr. J. Phys.*, 2019, **64**, 406.
30 Y. Joo Cho, K. Soo Yook, J. Yeob Lee, Y. J. Cho, K. S. Yook and J. Y. Lee, *Adv. Mater.*, 2014, **26**, 6642–6646.
31 E. G. Cansu-Ergun, *Polym. Rev.*, 2018, **58**, 42–62.
32 C. Tardío, J. Álvarez Conde, A. M. Rodríguez, P. Prieto, A. de la Hoz, J. Cabanillas-González and I. Torres-Moya, *Molecules*, 2023, **28**, 4631.
33 J. Jayabharathi, G. Goperundevi, V. Thanikachalam and S. Panimozhi, *ACS Omega*, 2019, **4**, 15030–15042.
34 W. C. Chen, Z. L. Zhu and C. S. Lee, *Adv. Opt. Mater.*, 2018, **6**, 1800258.
35 J. Jayabharathi, J. Anudeebhana, V. Thanikachalam and S. Sivaraj, *RSC Adv.*, 2020, **10**, 8866–8879.
36 J. Tagare and S. Vaidyanathan, *J. Mater. Chem. C*, 2018, **6**, 10138–10173.
37 Y. Liu, T. Tao, H. C. Hu, H. Li and X. Ouyang, *Dyes Pigm.*, 2021, **188**, 109191.
38 Y. H. Gao, C. Chen, Q. Tang, B. Su, G. Zhang, B. X. Bo and W. L. Jiang, *J. Mater. Sci.: Mater. Electron.*, 2017, **28**, 7204–7211.
39 C. Liu, T. Li, M. Sun, M. Xie, Y. Zhou, W. Feng, Q. Sun, S.-T. Zhang, S. Xue, W. Yang, C. Liu, T. Li, M. Sun, M. Xie, Y. Zhou, W. Feng, Q. Sun, S. Xue, W. Yang and S.-T. Zhang, *Adv. Funct. Mater.*, 2023, **33**, 2215066.
40 T. Hu, Y. Guo, G. Han and Y. Yi, *J. Phys. Chem. C*, 2024, **128**, 3148–3154.
41 C. Mayr and W. Brütting, *Chem. Mater.*, 2015, **27**, 2759–2762.
42 S. Sohn, M. J. Kim, S. Jung, T. J. Shin, H. K. Lee and Y. H. Kim, *Org. Electron.*, 2015, **24**, 234–240.
43 D. Yokoyama, *J. Mater. Chem.*, 2011, **21**, 19187–19202.
44 C. K. Moon, K. H. Kim, J. W. Lee and J. J. Kim, *Chem. Mater.*, 2015, **27**, 2767–2769.
45 T. Marcato and C. J. Shih, *Helv. Chim. Acta*, 2019, **102**, e1900048.
46 T. Chatterjee and K. T. Wong, *Adv. Opt. Mater.*, 2019, **7**, 1800565.
47 Y. Liu, M. Nishiura, Y. Wang and Z. Hou, *J. Am. Chem. Soc.*, 2006, **128**, 5592–5593.
48 S. Macionis, D. Gudeika, D. Volyniuk, O. Bezvikonnyi, V. Andruleviciene, J. Haw Lee, B.-A. Fan, C.-H. Chen, B.-Y. Lin, T.-L. Chiu and J. V. Grazulevicius, *Adv. Opt. Mater.*, 2021, **9**, 2002227.
49 S. H. Cheng, W. Y. Hung, M. H. Cheng, H. F. Chen, A. Chaskar, G. H. Lee, S. H. Chou and K. T. Wong, *J. Mater. Chem. C*, 2014, **2**, 8554–8563.
50 S. Y. Chang, G. T. Lin, Y. C. Cheng, J. J. Huang, C. L. Chang, C. F. Lin, J. H. Lee, T. L. Chiu and M. K. Leung, *ACS Appl. Mater. Interfaces*, 2018, **10**, 42723–42732.
51 Y. M. Huang, T. Y. Chen, D. G. Chen, H. C. Liang, C. H. Wu, M. M. Lee, T. L. Chiu, J. H. Lee, Y. C. Chiu, P. T. Chou and M. K. Leung, *J. Mater. Chem. C*, 2021, **9**, 2381–2391.
52 A. Kundu, S. Karthikeyan, Y. Sagara, D. Moon and S. P. Anthony, *ACS Omega*, 2019, **4**, 5147–5154.
53 J. Jayabharathi, R. Ramya, V. Thanikachalam, P. Jeeva and E. Sarojpurani, *RSC Adv.*, 2019, **9**, 2948–2966.
54 J. Jayabharathi, V. Thanikachalam, R. Ramya and S. Panimozhi, *RSC Adv.*, 2019, **9**, 33693–33709.
55 S. Arunlimsawat, P. Funchien, P. Chasing, A. Saenubol, T. Sudyoadsuk and V. Promarak, *Beilstein J. Org. Chem.*, 2023, **19**, 1664–1676.
56 T. Serevičius, R. Skaisgiris, J. Dodonova, L. Jagintavičius, D. Banevičius, K. Kazlauskas, S. Tumkevičius and S. Juršėnas, *ACS Appl. Mater. Interfaces*, 2020, **12**, 10727–10736.
57 M. Mamada, H. Katagiri, C. Y. Chan, Y. T. Lee, K. Goushi, H. Nakanotani, T. Hatakeyama and C. Adachi, *Adv. Funct. Mater.*, 2022, **32**, 2204352.
58 K. Stavrou, L. G. Franca, A. Danos and A. P. Monkman, *Nat. Photonics*, 2024, **18**, 554–561.